Supplementary Material

Urban surface-atmosphere fluxes of pptv-level oxygenated organic molecules (OOMs) from eddy covariance observations

Jieya Sun[1], Xinyu Wang[1], Jingya Hua[1], Bo Zhu[2], Nan Chen[1], Huan Yu[1*]

1. Department of Atmospheric Science, School of Environmental Studies, China University of Geosciences, Wuhan 430074, China
2. Hubei Ecological Environment Monitoring Center Station, Wuhan 430070, China

Correspondence: Huan Yu, yuhuan@cug.edu.cn

Text S1-S11

Figure S1-S11

Table S1

Text S1. Peak fitting of target OOMs

Daily mass calibration was conducted using NO_3^-, $C_2F_3O_2^-$, I^-, IH_2O^-, $ICH_2O_2^-$, $IHNO_3^-$, and I_3^- ions, covering a mass range of 62–381 m/q. Raw I-CIMS spectra were iteratively fitted with multiple peaks using a custom-defined peak shape until residuals fell below 5%. Exact masses of the fitted peaks were then assigned to the most probable elemental formulas within the range $C_{1\text{-}30}H_{1\text{-}60}O_{0\text{-}20}N_{0\text{-}2}S_{0\text{-}2}X_{0\text{-}2}I_{0\text{-}1}^-$(X denotes halogen atoms), with a mass error tolerance of <10 ppm at an instrumental mass resolution of ~6000. Priority was given to formulas corresponding to atmospherically relevant OOM formulas well-documented in the peer-reviewed literature. Isotopic distributions were verified to be consistent with theoretical patterns. Additional constraints included elemental ratios ($0.3 \leq H/C \leq 3$, $N/C \leq 0.5$, $O/C \leq 3$, $S/C \leq 1$) and double bond equivalent (DBE) limits ($0 \leq DBE \leq 20$). This procedure yielded more than 400 ion formulas, for which 10 Hz time series were generated and normalized to counts per second per one million reagent ions (that is, the sum of I^- and IH_2O^-).

Text S2. Determination of Maximum Sensitivity (S_{max}) of the Iodide-CIMS

Iodide-adduct ions ($M \cdot I^-$) are formed via collisions between neutral OOM molecules and the iodide reagent ion (I^-) in the CIMS ion-molecule reaction (IMR) chamber. The maximum sensitivity (S_{max}) represents the instrument's upper detection limit for compounds that form iodide adducts at the collision limit with negligible declustering. On basis of quantum mechanical calculations and experimental measurements, Iyer et al. (2016) identified malonic acid ($C_3H_4O_4$), succinic acid ($C_4H_6O_4$), levoglucosan ($C_6H_{10}O_5$), and methyl erythritol ($C_7H_{14}O_5$) as kinetically limited compounds. In this work, levoglucosan was used to determine S_{max} using a thermal desorption approach with FIGAERO-I-CIMS:

(1) A 20 ppm levoglucosan stock solution was prepared in acetone/methanol (9:1, v/v).

(2) 2.5 μL stock aliquots were deposited onto PTFE filter punches and analyzed by FIGAERO-I-CIMS with a thermal program: 20→200 °C over 15 min, 200 °C hold for

15 min, cool to 20 °C over 10 min. Blank runs with the same program were used for background subtraction. This procedure was repeated in triplicate.

(3) The procedure was repeated for 5 μL and 7.5 μL stock aliquots.

(4) In-field calibration was conducted throughout the analysis, with one levoglucosan standard run every 10 samples to monitor instrument stability.

Assuming complete vaporization of levoglucosan from the filter punches during thermal desorption, the integrated signal response was calculated to be (1.76 ± 0.12) × 10^5 counts ng^{-1}. Next, the gaseous sensitivity of levoglucosan ($S_{C6H10O5,g}$, units: cps $pptv^{-1}$) was derived. The total integrated signal generated during the desorption of 1 ng levoglucosan is given by $signal = \int S_{C6H10O5,g} \frac{m_t/M_x}{Q_t/V_{std}} dt$, where m_t is the instantaneous evaporation rate of levoglucosan, Q_t is the constant nitrogen carrier gas flow rate (1.8 SLPM), V_{std} is the standard molar volume of an ideal gas at STP (22.4 L mol^{-1}), and M_x is the molar mass of levoglucosan (162 g mol^{-1}). Rearranging yields $S_{C6H10O5,g} = \frac{signal/\int m_t dt}{V_{std}/(M_x Q_t)}$. Substituting the measured response factor $signal/\int m_t dt$ (1.76 ± 0.12) × 10^5 counts ng^{-1} gives $S_{C6H10O5,g}$ = 38 ± 2.6 cps $pptv^{-1}$.

The gaseous sensitivity of levoglucosan is related to the maximum instrument sensitivity by $S_{C6H10O5,\ g} = S_{max} \times 1/S_0 \times T_M$, where $1/S_0 \approx 1$ for levoglucosan (negligible adduct dissociation), and $T_{C6H10O5}$ = 1.365 (mass-dependent transmission efficiency, calculation detailed in Text S4). Thus, the maximum instrument sensitivity was determined as S_{max} = 27.8 ± 1.9 cps $pptv^{-1}$.

Text S3. The sensitivity of a compound M relative to maximum sensitivity ($1/S_0$)

During transmission through the electric fields to the time-of-flight mass spectrometer (TOF-MS), $M{\cdot}I^-$ adducts undergo partial dissociation. The relative sensitivity ($1/S_0$) of a given compound M is controlled by the binding energy of its $M{\cdot}I^-$ cluster. More strongly bound clusters are more likely to remain intact during ion transmission and thus yield higher apparent sensitivity, whereas weakly bound clusters tend to dissociate prior to detection, reducing sensitivity. Iyer et al. (2016) demonstrated a logarithmic linear relationship between the $M{\cdot}I^-$ cluster binding energy and the

observed sensitivity. Although quantum chemical calculations can, in principle, provide binding energies for $M \cdot I^-$ clusters, they are computationally demanding and difficult to apply to compounds with unknown structures. To constrain sensitivities for a broader range of detected compounds in the absence of standards, Lopez-Hilfiker et al. (2016) proposed an experimental de-clustering approach.

In our CIMS, the voltage difference ΔV between the skimmer (SSQ) and the entrance to the big segmented quadrupole (BSQ, Q2 front) is set to 3 V during regular operation. Following Lopez-Hilfiker et al. (2016), we carried out de-clustering scans by programmatically ramping ΔV from 3 to 30 V during online measurements. Scans were conducted in four time windows (morning, afternoon, evening, and midnight), with three 10-minute scans in each window. For every iodide cluster ion $M \cdot I^-$, we calculated the fraction of signal remaining at each ΔV relative to its signal at ΔV = 3 V and plotted this remaining fraction as a function of ΔV (examples are shown in Figure S3a).

The dependence of remaining signal fraction on ΔV follows a sigmoidal function. We therefore fitted a sigmoid to the data for each $M \cdot I^-$ cluster and obtained two parameters, S_0 and dV_{50}. Here, S_0 is the maximum signal of the sigmoid (normalized to the signal at ΔV = 3 V), occurring at the low-ΔV end of the curve, and dV_{50} is the voltage difference at which the cluster signal drops to half of this maximum.

Figure S3b summarizes the dV_{50} and $1/S_0$ values for all observed clusters. The data display a sigmoidal relationship, which is highly consistent with the curves reported in Lopez-Hilfiker et al. (2016) and Ye et al. (2021). The $1/S_0$ value reaches a plateau at $dV_{50} \approx 13$ V, corresponding to the maximum effective sensitivity of the instrument. The dV_{50} values of the selected OOMs are tightly clustered around this plateau and its inflection point, as these species form adducts with strong binding strength and minimal dissociation. Here, dV_{50} is used to quantify the relative sensitivity of the selected OOMs normalized to the maximum sensitivity, with all measured values falling within ±11% of the sigmoidal fit (defined by Equation S1 and illustrated in Figure S3b).

$$1/S_0 = 0.27326 + \frac{0.68617}{1+\exp\left(\frac{5.5309-dV_{50}}{3.007}\right)}. \qquad \text{(S1)}$$

Text S4. Mass dependent transmission

The transmission of ions through a mass spectrometer is inherently mass dependent because ions must pass through a series of electric and magnetic fields whose focusing and guiding efficiencies vary with mass-to-charge ratio (m/q). To correct for this effect in our TOF-CIMS, we assumed a transmission efficiency of 1 for I^- and expressed the transmission efficiency of each $M{\cdot}I^-$ cluster relative to that of I^-; the transmission efficiency of $M{\cdot}I^-$ is denoted as T. We adopted the empirical mass-dependent transmission correction developed by Isaacman-VanWertz et al. (2018), which derives transmission directly from the CIMS dataset without requiring external standards. The method is based on the matrix equation (Equation S2):

$$\begin{bmatrix} I_{11} & I_{12} & \cdots & I_{1n} \\ I_{21} & I_{22} & \cdots & I_{2n} \\ \vdots & \vdots & \ddots & \vdots \\ I_{m1} & I_{m2} & \dots & I_{mn} \end{bmatrix} \cdot \begin{bmatrix} 1/T_1 \\ 1/T_2 \\ \vdots \\ 1/T_n \end{bmatrix} = \begin{bmatrix} I_0 \\ I_0 \\ \vdots \\ I_0 \end{bmatrix} \qquad \text{(S2)}$$

where I_{ij} is the signal intensity of the jth m/q in the ith spectrum, $1/T_j$ is the reciprocal of the transmission efficiency at the jth m/q, and I_0 is the TIC that would be observed under ideal, mass-independent transmission.

Following Isaacman-VanWertz et al. (2018), we solved Equation S2 using both a linear least squares approach and a constrained functional fit. In the linear least-squares method, the transmission at each nominal mass is treated as independent and is obtained by minimizing the difference between the modeled and observed TIC. While this efficiently handles large datasets and automatically yields a best-fit solution, the resulting T(m/q) curve is noisy, especially in the presence of multicollinearity among mass channels.

In contrast, the constrained-function method assumes that the mass-dependent transmission can be described by a smooth functional form. Specifically, we assumed that T as a function of m/q follows a Gaussian-like distribution (Heinritzi et al., 2016) and optimized the function parameters to minimize the variability of TIC across the dataset. This yields a smooth, physically reasonable transmission curve and reduces both noise and overfitting, although the accuracy depends on the appropriateness of the

chosen functional form. The resulting transmission function is shown in Figure S4.

Based on the constrained-function fit, we obtained the following Gaussian transmission parameterization for $M \cdot I^-$ clusters:

$$T_M = 0.21432 + 1.201 \times e^{-\left(\frac{m/q-249.3}{189.5}\right)^2} \quad \text{(S3)}$$

which was used to correct the mass-dependent transmission of all ions in this study.

We estimated T_M uncertainty using 1000 bootstrap resamplings, refitting the Gaussian transmission curve each time. For OOMs and HNO_3 (m/q 173–287), the 1σ precision is 10%–30%.

Text S5. Response factor calculation and uncertainty estimation

The mixing ratio of an OOM species [M] (in pptv) is calculated as:

$$[M] = \frac{I}{S_{max} \times 1/S_0 \times T_M} \quad (1)$$

where I is the normalized $M \cdot I^-$ ion signal (counts per second, cps, normalized to 10^6 reagent ions). From the calibration experiments described above, the measurement precision (1σ) of the maximum sensitivity S_{max}, relative sensitivity $1/S_0$, and mass-dependent transmission T_M were determined to be 6.8%, 11%, and 10–30%, respectively. Following Gaussian error propagation, the combined measurement precision of the response factor $S_{max} \times 1/S_0 \times T_M$ from our collision limit-constrained sensitivity calibration method was calculated to be 33–65% (2σ, 95% confidence interval), depending on the target species.

To validate this approach, we performed direct calibration using nitric acid and formic acid from Kintek permeation tubes with certified emission rates. The standard gases were generated by diluting the permeation tube effluent with high-purity nitrogen, covering target concentrations of 0.1, 0.5, and 1.0 ppbv. Direct calibration via I-CIMS yielded calibration factors of 25 cps/pptv for nitric acid and 36 cps/pptv for formic acid. These values fall within the ±33% (2σ) precision range of the response factors derived from our collision-limited sensitivity method. To maintain consistency, we used the response factors provided in Table S1 to quantify all the OOMs and nitric acid.

Text S6. Raw data pre-processing

Prior to eddy covariance flux calculations, all 10 Hz raw data (including wind components, sonic temperature, and gas concentrations) must undergo rigorous pre-processing to ensure physical integrity and measurement accuracy.

First, horizontal coordinate rotation is performed to correct for geographic azimuth bias. The raw wind components (u, v, w) measured by the Campbell Scientific CSAT3B 3D sonic anemometer are inherently referenced to its internal instrument coordinate system. A 2D orthogonal rotation matrix is constructed using the precisely measured azimuth angle of the probe head relative to true north, and linear algebraic projection is applied to the raw horizontal wind components to map them into the geographic coordinate system, yielding geophysically meaningful wind components.

Second, a double coordinate rotation is applied to eliminate biases caused by instrument installation tilt and topographic undulations, ensuring the time-averaged vertical wind velocity equals zero. The procedure follows these steps: (1) Calculate the mean wind vector ($\bar{u}$, $\bar{v}$, $\bar{w}$) from the 10 Hz raw wind data over each 30-minute averaging period (18,000 samples total). Perform the first rotation around the z-axis to set $\bar{v} = 0$, determining the yaw angle. (2) Perform the second rotation around the newly defined y-axis to set $\bar{w} = 0$, determining the pitch angle. The resulting rotated $\bar{u}$ represents the mean wind speed for the period. (3) Construct a combined rotation matrix from the two angles and apply it sample-wise to all instantaneous raw data points in the 30-minute interval, generating the corrected wind time series (u_{rot}, v_{rot}, w_{rot}). This ensures subsequent Reynolds decomposition is performed on turbulent fluctuations perpendicular to the local mean flow streamline.

Third, raw data are cleaned and quality controlled following the standard protocol of Vickers & Mahrt (1997): (1) Despiking: A 5-minute sliding window is used to scan the time series. Isolated spikes or short consecutive spikes (<3 samples) exceeding the threshold of mean ± 3.5 standard deviations are identified and removed to eliminate electronic noise and physical interference. (2) Non-destructive statistical quality tests: a suite of standardized tests that each generate a per-variable binary quality flag (0 =

pass, 1 = fail) is conducted to assess data integrity: these include the amplitude resolution test to detect periods where signal variance is too low relative to instrument digitization resolution, the drop-outs test to identify short intervals where the signal sticks to a non-physical constant value, the absolute limits test to flag values outside physically plausible ranges for each variable, the skewness and kurtosis test to detect anomalous probability distributions indicative of instrument malfunction, the discontinuity test to identify non-physical semi-permanent step changes in the signal, and the steadiness of horizontal wind test to evaluate the stationarity of horizontal wind fields over the averaging period. Any 30-minute averaging period with a failed flag for any critical variable (wind components, sonic temperature, or target species) is excluded from subsequent flux calculations.

Text S7. Lag Time Determination

Actual lag times of gas concentrations relative to vertical wind speed were determined via the maximum covariance method. A theoretical nominal time lag (T_{nom} = 1.11 s) was first calculated from closed-path system parameters (inlet length, inner diameter, sample flow rate) as $T_{nom} = \frac{tube\ length \times tube\ cross\ section}{flowrate}$).

An asymmetric 0 - 3.6 s search window ($3 \times T_{nom}$) was defined to accommodate potential lag increases from tube adsorption or flow fluctuations. The scalar time series was shifted point-by-point within this window to compute cross-covariances between vertical wind fluctuations (w') and concentration fluctuations (c'). The time shift yielding the maximum absolute cross-covariance was adopted as the optimal 30-minute lag. If the optimal lag fell at window boundaries, the nominal lag was used to avoid spurious peak matches from poor data quality.

Text S8. Steady-State Test and Integral Turbulence Characteristics Test

Half-hourly flux quality was assessed using the standardized Steady-State Test (SST) and Integral Turbulence Characteristics (ITC) Test per Foken et al. (2004).

The SST evaluates flux stationarity by comparing the full 30-minute flux with the arithmetic mean of fluxes calculated from six non-overlapping 5-minute sub-intervals.

A relative difference <30% denotes high quality, 30–60% acceptable quality, and >60% poor quality.

The ITC test verifies compliance with flux-variance similarity theory (FVST), which states that the normalized standard deviation of a scalar ($\sigma_X / |X^*|$) depends solely on atmospheric stability, where $X^* = \overline{w'X'}/u^*$ is the characteristic scalar scaling parameter, w′X′ is the vertical scalar flux, and u^* is friction velocity. Theoretical values of $\sigma_X / |X^*|$ are parameterized as $c1(\frac{z}{L})^{c2}$, where $\frac{z}{L}$ is the dimensionless Monin-Obukhov stability parameter (z = measurement height above zero-plane displacement, L = Obukhov length), and $c1$, $c2$ are empirical constants for unstable, neutral, and stable conditions. Quality is graded by relative deviation between measured and theoretical normalized variances: <30% (high quality, well-developed turbulence), 30-100% (acceptable), and >100% (poor quality, severe flow distortion or non-turbulent conditions).

A quality flag (0 = good, 1 = acceptable, 2 = poor) was assigned to each flux interval. Only flags 0 and 1 were retained for subsequent analysis.

Text S9. Random Sampling Error of Flux

Because atmospheric turbulence is inherently chaotic and stochastic, eddy covariance flux measurements are unavoidably subject to random sampling error. This random uncertainty is primarily controlled by the number of statistically independent turbulent samples that can be captured within the flux averaging period (30 min). Therefore, before quantifying the flux random uncertainty due to sampling error, we first determined the integral turbulence time scale (ITS). The ITS characterizes the mean correlation time of turbulent eddies, i.e., the effective duration over which two time series (vertical wind velocity w and a scalar c) remain correlated. A smaller ITS indicates a shorter correlation time and thus a shorter mean eddy lifetime, implying that more independent turbulent realizations are sampled within 30 minutes and the random flux error is reduced.

The ITS is defined as the integral of the normalized cross-covariance function $R_{wc}(\tau)$:

$$R_{wc}(\tau) = \overline{w'(t)c'(t+\tau)} \quad \text{(S4)}$$

$$ITS = \frac{1}{\overline{w'c'}} \int_0^{+\infty} R_{wc}(\tau) d\tau \quad \text{(S5)}$$

where *w* is the vertical wind component, *c* is an arbitrary scalar (e.g., temperature or gas concentration), *t* denotes time within the averaging window (0-30 min), and τ is the lag between the two time series. The cross-covariance $R_{wc}(\tau)$ attains its maximum at τ = 0 and generally decays with increasing τ. Following common eddy covariance practice, we defined a finite upper integration limit by identifying the time at which the cross-covariance $R_{wc}(\tau)$ normalized by $\overline{w'c'}$ first decays to 1/e (≈ 0.369).

Given the ITS, the random flux uncertainty σF is estimated from the variance of the covariance following Finkelstein & Sims (2001):

$$\sigma F = \frac{1}{\sqrt{n}} \left(\sum_{p=-m}^{m} \gamma_{w,w}(p) \gamma_{c,c}(p) + \sum_{p=-m}^{m} \gamma_{c,w}(p) \gamma_{c,w}(p) \right)^{1/2} \quad \text{(S6)}$$

where *n* is the total number of samples within the 30-minute averaging period (18,000 points), and m is the discrete lag index corresponding to the ITS (m = ITS × sampling frequency). $\gamma_{w,w}(p)$ is the autocovariance function of vertical wind speed w at lag p, $\gamma_{c,c}(p)$ is the autocovariance function of scalar c, and $\gamma_{c,w}(p)$ is the cross-covariance between *c* and *w*.

The resulting σ_F represents the standard deviation of the flux estimate due to random sampling over the 30-minute period. Thus, the true flux value lies within the interval $F \pm \sigma_F$ at approximately the 68% confidence level.

Text S10. Low Frequency Flux Correction

Low-frequency losses in eddy covariance fluxes arise from the finite averaging period (30 min) and from detrending procedures (e.g., running mean, linear detrending), both of which act as high-pass filters that remove contributions from large, slowly varying turbulent structures. We quantified these losses using the analytical approach of J. Moncrieff et al. (2004).

This method constructs an ideal, unattenuated theoretical cospectrum $CO_F(f)$ following the Kaimal et al. (1972) model, using site-specific atmospheric conditions

for each 30-minute interval: stability parameter *z/L*, mean horizontal wind speed, and measurement height . A high-pass transfer function HPTF(*f*) is then derived to represent the combined attenuation from detrending and the finite sampling window. The high-pass spectral correction factor (HPSCF) is defined as the ratio of the total unattenuated flux to the attenuated flux:

$$HPSCF = \frac{\int_0^{fmax} CO_F(f)df}{\int_0^{fmax} CO_F(f)\times HPTF(f)df} \quad \text{(S7)}$$

A key feature of this analytical method is that the correction factor is identical for all scalars within a given 30-minute period, as it depends only on atmospheric stability and measurement geometry, not on scalar properties. In this study, HPSCF values ranged from 1.01 to 1.53, with a mean of 1.13 ± 0.07.

The relative low-frequency flux loss ΔF/F is calculated as

$$\frac{\Delta F}{F} = 1 - \frac{1}{HPSCF} \quad \text{(S8)}$$

The resulting relative losses ranged from 0.6% to 34.7%, with an average of 11.5% ± 5.3%.

Text S11. High Frequency Flux Correction

High-frequency attenuation in closed-path eddy covariance systems arises from instrument response, path averaging, sensor separation, and inlet tube smearing. Unlike low-frequency correction, high-frequency attenuation is species-specific, primarily due to differences in wall adsorption-desorption kinetics and instrument response times for different compounds (Liu et al., 2019).

Two main approaches are commonly used for high-frequency correction:

1. The theoretical method of J. B. Moncrieff et al. (1997), which explicitly models each attenuation process. However, this method requires precise knowledge of system response times, which could not be accurately determined in this study due to the long PFA inlet, complex species-dependent wall interactions, and fluctuations in sampling flow rate.

2. The empirical field-based method of Ibrom et al. (2007), which assumes spectral similarity and uses the variance-normalized sonic temperature spectrum (unaffected by high-frequency attenuation) as a proxy for the ideal unattenuated scalar spectrum. This method was adopted here as it directly accounts for compound-specific attenuation without requiring a priori knowledge of system response functions.

Mathematically, the transfer function describing high-frequency attenuation is approximated as a first-order infinite impulse response (IIR) filter with a Lorentzian form:

$$H_{IIR}(f|f_c) = \frac{S_m(f)}{S(f)} = \frac{1}{1+(f/f_c)^2} \qquad \text{(S9)}$$

where f is frequency (Hz), f_c is the cutoff frequency (Hz) of the transfer function, S (f) is the variance-normalized sonic temperature power spectrum, and $S_m(f)$ is the noise-corrected variance-normalized power spectrum of the measured scalar (Figure 1c).

The cutoff frequency f_c is determined for each species by fitting Equation S9 to the measured spectra. The low-pass spectral correction factor (LPSCF) is then calculated using the parameterization:

$$LPSCF = \frac{d_1 u}{d_2 + f_c} + 1 \qquad \text{(S10)}$$

where u is the mean horizontal wind speed, and d_1 and d_2 are empirical parameters derived by fitting the low-pass attenuation of the sonic temperature cospectrum under different effective cutoff frequencies:

$$\frac{\overline{w'T_s'}}{\overline{w'T_{s,f}'}} = \frac{d_1 u}{d_2 + f_c} + 1 \qquad \text{(S11)}$$

where $\overline{w'T_s'}$ is the unfiltered sonic temperature flux, and $\overline{w'T_{s,f}'}$ is the sonic temperature flux filtered by a first-order IIR filter with cutoff frequency f_c. Further details of the method are given in Ibrom et al. (2007).

The resulting LPSCF values and corresponding high-frequency flux losses for HNO_3 and the selected OOM species are summarized in Table 1.

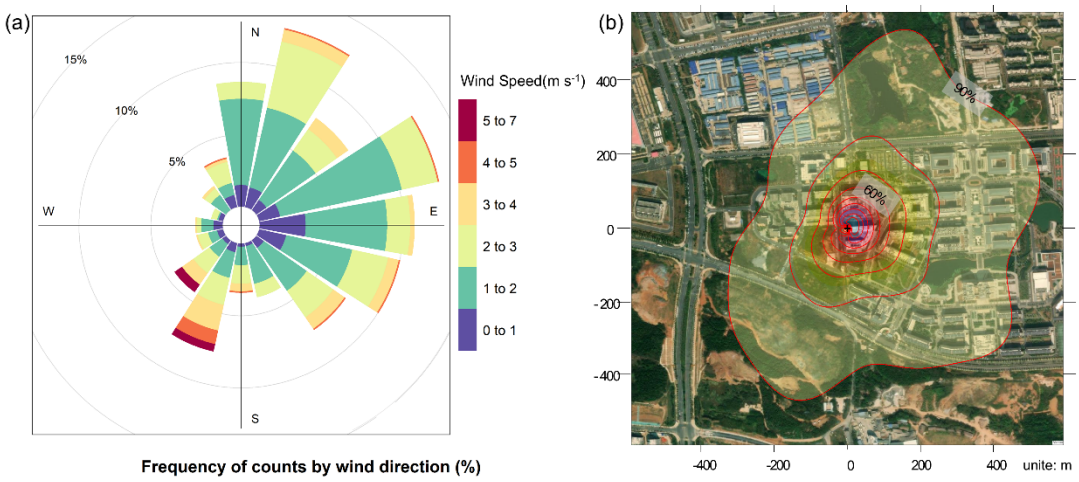

Figure S1. (a) Wind conditions during the entire campaign: wind direction frequency (% of time) color-coded by wind speed. (b) Average flux footprint for the entire campaign overlaid on a satellite base map (200×200 m grid, axes: distance from station), calculated for 30-min intervals using the 2D model of Kljun et al. (2015). Red contours (10–90%, 10% steps) show cumulative source contributions; the black cross marks the site. The satellite base map is sourced from Ovital Map (Omap) and is used for non-commercial academic purpose only.

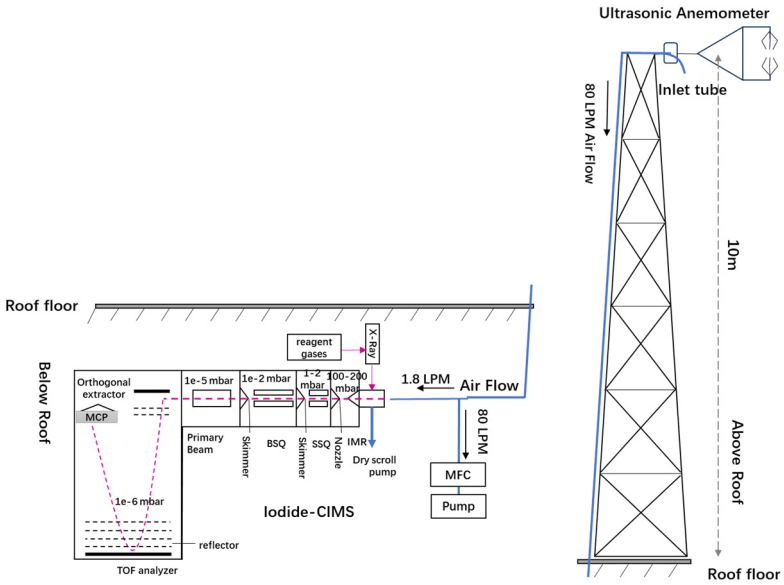

Figure S2. Schematic diagram of the eddy covariance observation system.

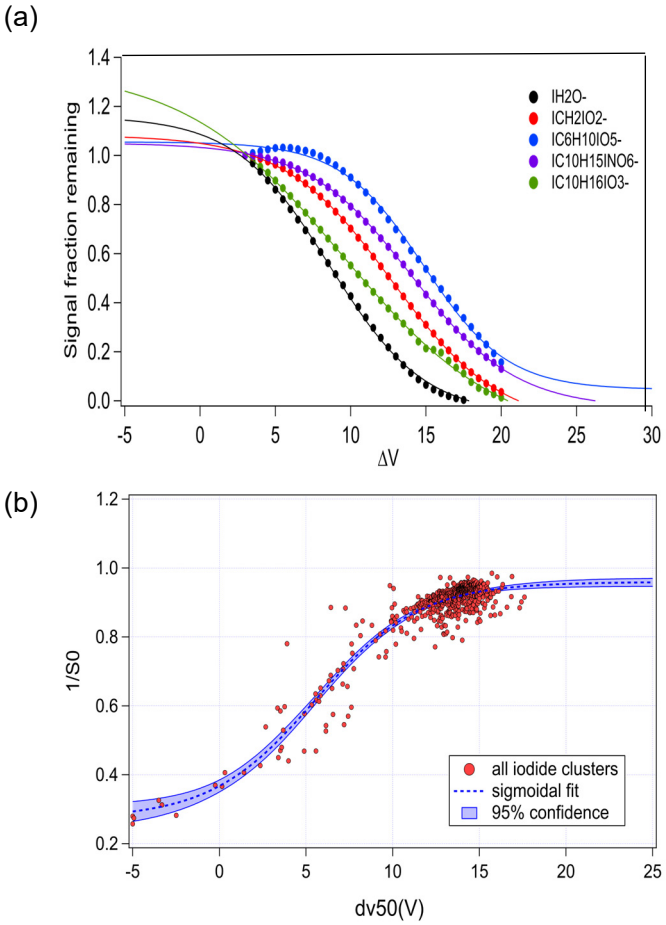

Figure S3. (a) The examples of de-clustering scans for some representative iodide cluster ions, showing the fraction of signal remaining at a given voltage difference ΔV relative to that at ΔV=3 V. Color curves are sigmoid fittings of the data points. **(b)** The sigmoidal fitting to the results of 1/S0 and dV50 obtained from de-clustering scans for all iodide adducts.

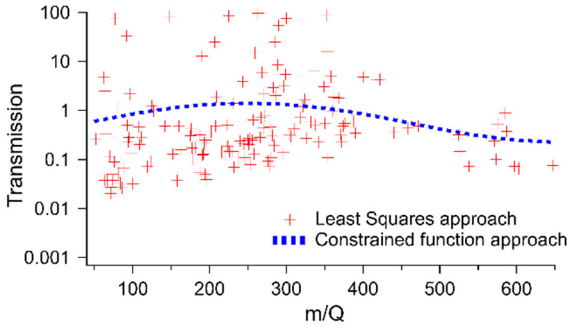

Figure S4. Mass dependent transmission coefficients solved by least squares approach (red plus signs) and constrained function approach (blue dashed line) obtained from atmospheric observation data of FIGAERO-I-CIMS.

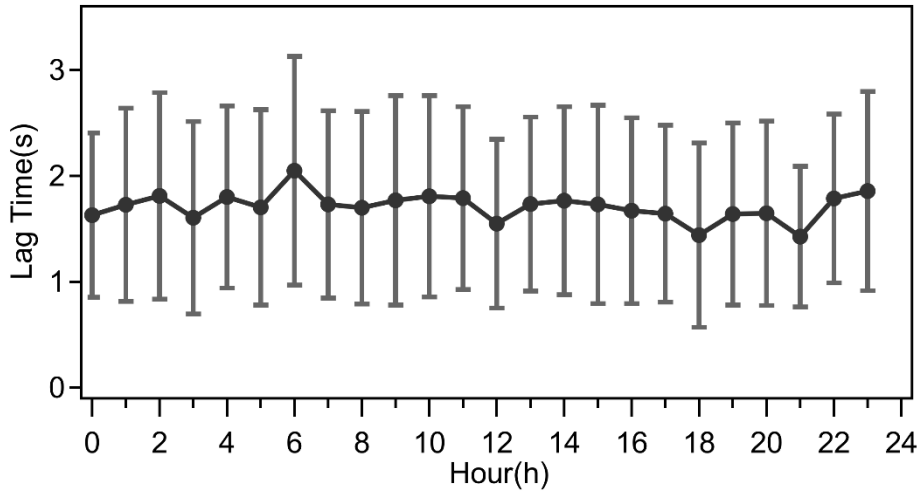

Figure S5. Mean diurnal variation of HNO_3 lag time during the measurement campaign. Error bars indicate day-to-day variability (standard deviation)

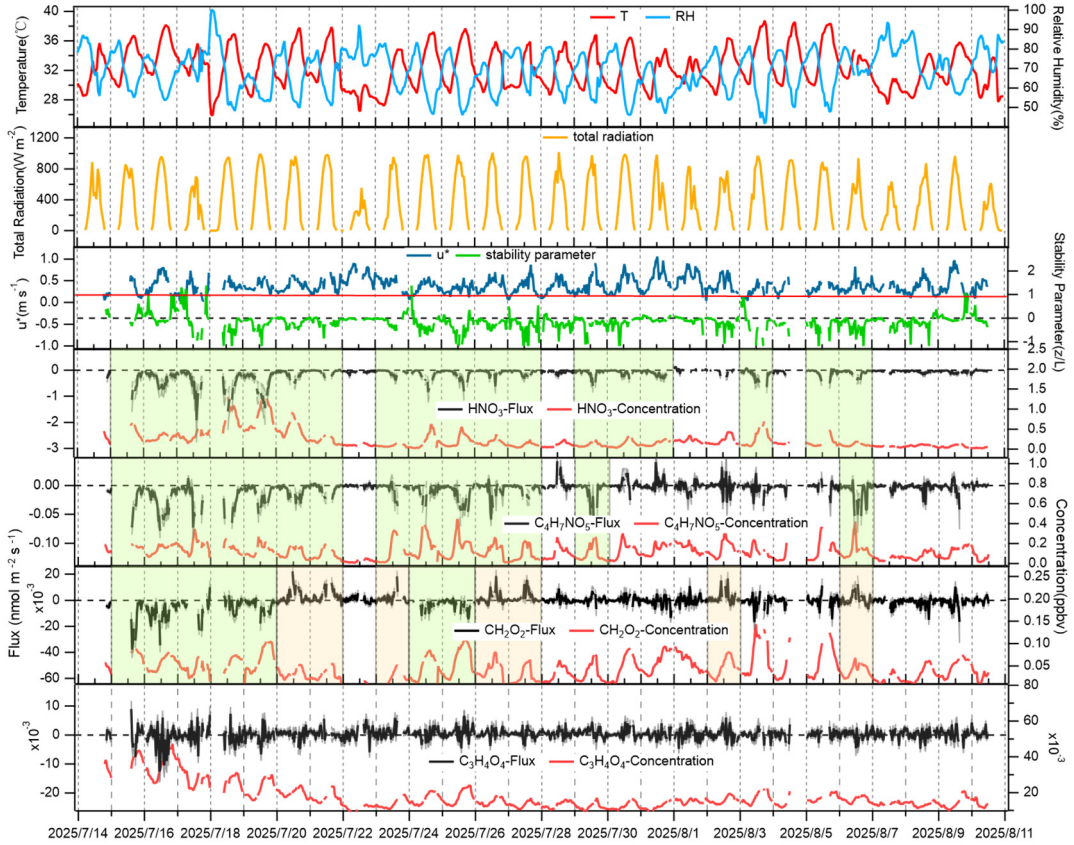

Figure S6. Time series of meteorological variables (temperature, relative humidity, total radiation, friction velocity (u*), stability parameter z/L), and fluxes and concentrations of species with varying SNRs (HNO_3, $C_4H_7NO_5$, CH_2O_2, $C_3H_4O_4$) during the measurement campaign. Black

dashed lines indicate the zero-level for each variable. The red solid line denotes the *u** threshold of 0.2 m/s. Green and orange shaded areas in the panels of HNO_3, $C_4H_7NO_5$, CH_2O_2 highlight negative flux days and positive flux days, respectively. Grey shaded area around the line denotes the corresponding random uncertainty of the flux estimates.

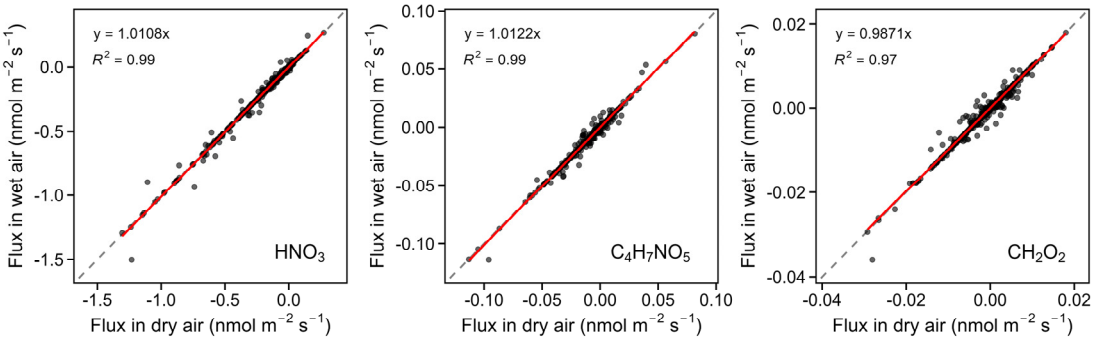

Figure S7. Correlation between fluxes calculated using wet mole fraction/wet air density and dry mole fraction/dry air density for species with varying SNRs. The gray dashed line represents the y=x reference.

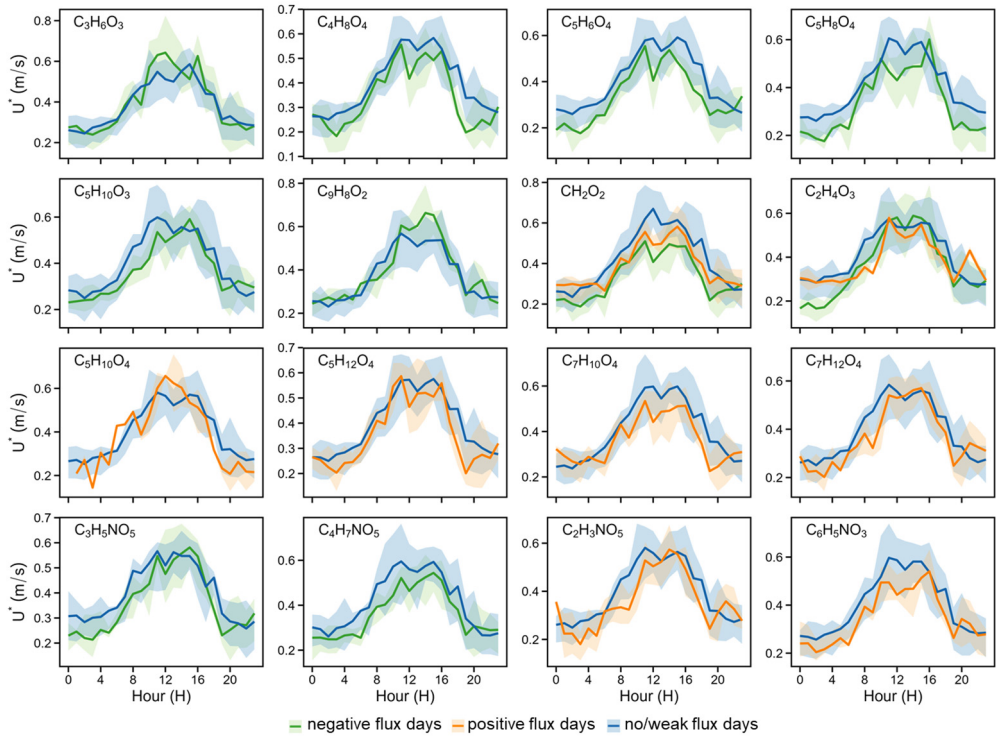

Figure S8. Diurnal cycles of friction velocity grouped by flux sign of OOMs: positive (orange), negative (green), and no/weak flux (blue) days. Shaded areas represent the corresponding 25th and

75th percentiles.

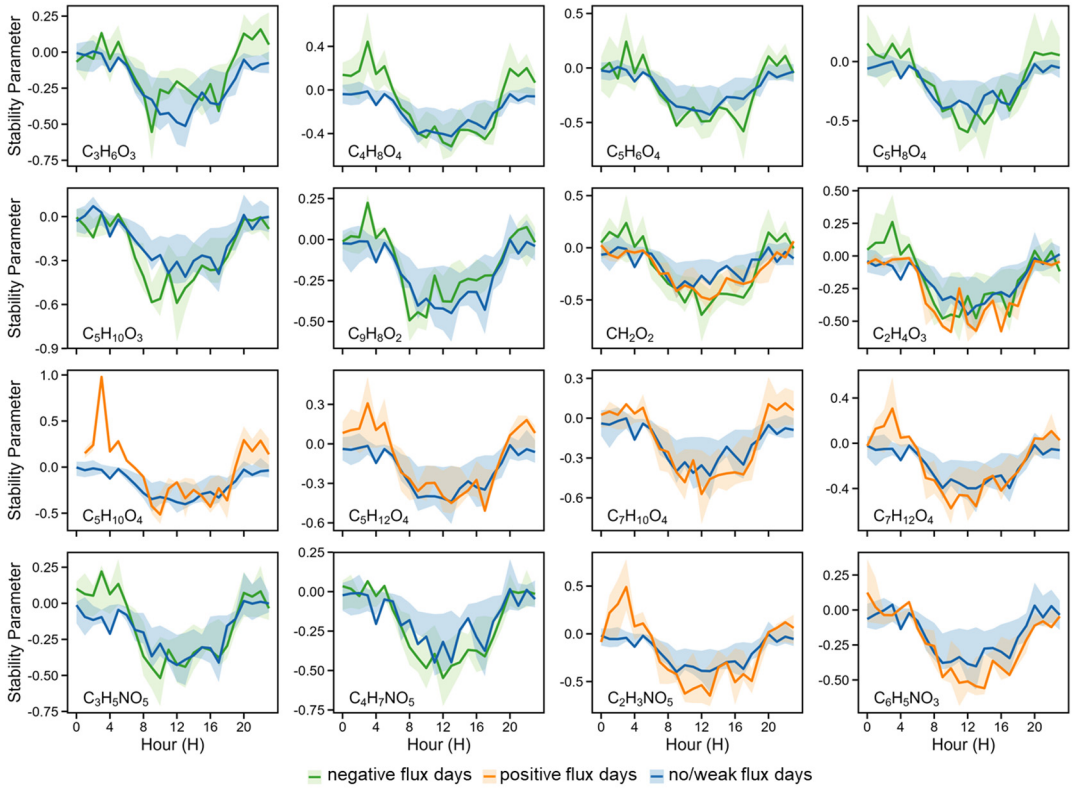

Figure S9. Diurnal cycles of stability parameter z/L grouped by flux sign of OOMs: positive (orange), negative (green), and no/weak flux (blue) days. Shaded areas represent the corresponding 25th and 75th percentiles.

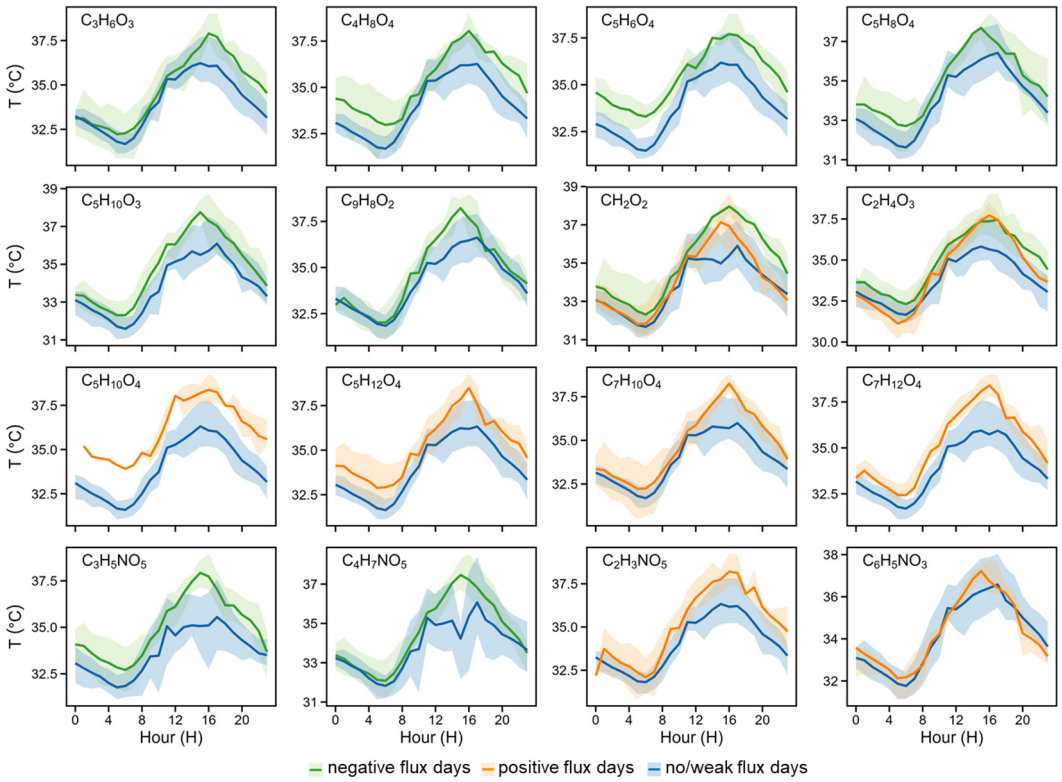

Figure S10. Diurnal cycles of temparature grouped by flux sign of OOMs: positive (orange), negative (green), and no/weak flux (blue) days. Shaded areas represent the corresponding 25th and 75th percentiles.

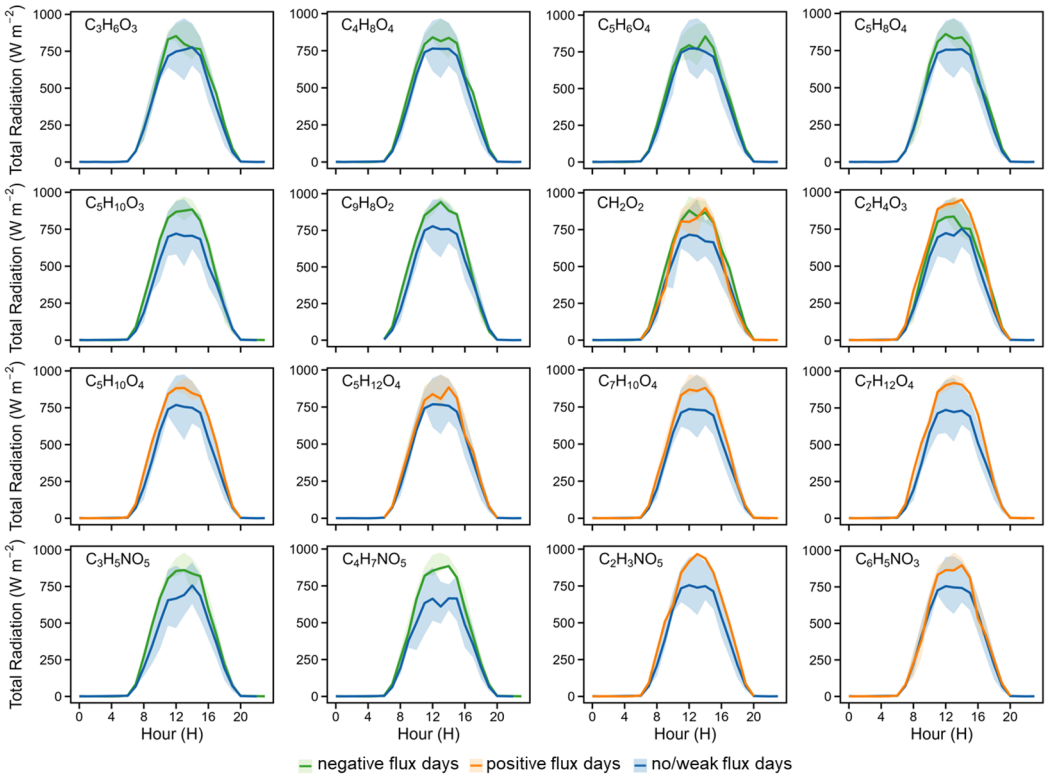

Figure S11. Diurnal cycles of total sun radiation grouped by flux sign of OOMs: positive (orange), negative (green), and no/weak flux (blue) days. Shaded areas represent the corresponding 25th and 75th percentiles.

Table S1 Detailed information of the 21 selected iodide-adduct ions. Fluxes were retrieved for the ions in bold.

No.	chemical formula	Response factor(cps/pptv)	T_X	S/N (10 Hz signal)	Mean detection limit (nmol m^{-2} s^{-1})	SCF
1	**$HINO_3^-$**	**34.75**	**1.30**	**9.88**	**0.75×10^{-2}**	**1.27±0.05**
2	**$C_4H_7INO_5^-$**	**37.24**	**1.39**	**5.71**	**0.52×10^{-2}**	**1.78±0.22**
3	**$C_2H_4IO_3^-$**	**35.9**	**1.35**	**5.12**	**1.62×10^{-3}**	**1.27±0.05**
4	**$C_5H_8IO_4^-$**	**39.31**	**1.41**	**4.69**	**1.75×10^{-3}**	**1.95±0.30**
5	**$C_5H_{10}IO_4^-$**	**39.28**	**1.41**	**4.33**	**1.48×10^{-3}**	**1.27±0.05**
6	**$C_7H_{10}IO_4^-$**	**38.24**	**1.37**	**3.96**	**1.65×10^{-3}**	**1.18±0.06**
7	**$C_3H_6IO_3^-$**	**37.08**	**1.38**	**3.87**	**1.98×10^{-3}**	**1.61±0.15**
8	**$CH_2IO_2^-$**	**32.77**	**1.24**	**3.67**	**2.12×10^{-3}**	**1.53±0.12**
9	**$C_5H_{10}IO_3^-$**	**37.23**	**1.41**	**3.67**	**2.65×10^{-3}**	**1.31±0.05**
10	**$C_5H_{12}IO_4^-$**	**31.87**	**1.41**	**3.46**	**1.74×10^{-3}**	**1.32±0.05**
11	$C_6H_{10}IO_4^-$	38.89	1.40	3.20	1.36×10^{-3}	1.18±0.06
12	**$C_6H_5INO_3^-$**	**39.15**	**1.41**	**3.19**	**2.38×10^{-3}**	**1.18±0.06**
13	**$C_5H_6IO_4^-$**	**37.46**	**1.41**	**2.97**	**1.22×10^{-3}**	**1.27±0.05**
14	**$C_2H_3INO_5^-$**	**39.40**	**1.42**	**2.98**	**0.98×10^{-3}**	**1.27±0.05**
15	**$C_4H_8IO_4^-$**	**36.06**	**1.42**	**2.96**	**1.06×10^{-3}**	**1.17±0.81**
16	**$C_7H_{12}IO_4^-$**	**38.10**	**1.37**	**2.81**	**1.22×10^{-3}**	**1.09±0.09**
17	$C_6H_8IO_4^-$	36.81	1.40	2.58	1.18×10^{-3}	1.15±0.07
18	**$C_9H_8IO_2^-$**	**35.36**	**1.32**	**2.40**	**1.05×10^{-3}**	**1.27±0.05**
19	**$C_3H_5INO_5^-$**	**37.57**	**1.41**	**2.21**	**1.27×10^{-3}**	**1.54±0.13**
20	$C_3H_4IO_4^-$	37.15	1.40	2.18	1.21×10^{-3}	1.18±0.06
21	$C_4H_6IO_4^-$	36.74	1.41	2.10	2.09×10^{-3}	1.27±0.05

References

Finkelstein, P. L., & Sims, P. F. (2001). Sampling error in eddy correlation flux measurements. *Journal of Geophysical Research: Atmospheres*, *106(D4)*, 3503-3509. https://doi.org/10.1029/2000JD900731

Foken, T., Göockede, M., Mauder, M., Mahrt, L., Amiro, B., & Munger, W. (2004). Post-field data quality control, In X. Lee, W. Massman & B. Law (Eds.), *Handbook of micrometeorology: A guide for surface flux measurement and analysis*,

Atmospheric and Oceanographic Sciences Library (Vol. 29, pp. 181-208). Springer, Dordrecht.

Heinritzi, M., Simon, M., Steiner, G., Wagner, A. C., Kürten, A., Hansel, A., & Curtius, J. (2016). Characterization of the mass-dependent transmission efficiency of a CIMS. *Atmospheric Measurement Techniques*, *9(4)*, 1449-1460. https://doi.org/10.5194/amt-9-1449-2016

Ibrom, A., Dellwik, E., Flyvbjerg, H., Jensen, N. O., & Pilegaard, K. (2007). Strong low-pass filtering effects on water vapour flux measurements with closed-path eddy correlation systems. *Agricultural And Forest Meteorology*, *147(3-4)*, 140-156. https://doi.org/10.1016/j.agrformet.2007.07.007

Isaacman-VanWertz, G., Massoli, P., O'Brien, R., Lim, C., Franklin, J. P., Moss, J. A., Hunter, J. F., Nowak, J. B., Canagaratna, M. R., & Misztal, P. K. (2018). Chemical evolution of atmospheric organic carbon over multiple generations of oxidation. *Nature Chemistry*, *10(4)*, 462-468. https://doi.org/10.1038/s41557-018-0002-2

Iyer, S., Lopez-Hilfiker, F., Lee, B. H., Thornton, J. A., & Kurten, T. (2016). Modeling the detection of organic and inorganic compounds using iodide-based chemical ionization. *Journal of Physical Chemistry A*, *120(4)*, 576-587. https://doi.org/10.1021/acs.jpca.5b09837

Kaimal, J. C., Wyngaard, J. C. J., Izumi, Y., & Coté, O. R. (1972). Spectral characteristics of surface-layer turbulence. *Quarterly Journal Of The Royal Meteorological Society*, *98(417)*, 563-589. https://doi.org/10.1002/qj.49709841707

Kljun, N., Calanca, P., Rotach, M. W., & Schmid, H. P. (2015). A simple two-dimensional parameterisation for Flux Footprint Prediction (FFP). *Geoscientific Model Development*, *8(11)*, 3695-3713. https://doi.org/10.5194/gmd-8-3695-2015

Liu, X., Deming, B., Pagonis, D., Day, D. A., Palm, B. B., Talukdar, R., Roberts, J. M., Veres, P. R., Krechmer, J. E., & Thornton, J. A. (2019). Effects of gas–wall interactions on measurements of semivolatile compounds and small polar molecules. *Atmospheric Measurement Techniques*, *12(6)*, 3137-3149. https://doi.org/10.5194/amt-12-3137-2019

Lopez-Hilfiker, F. D., Iyer, S., Mohr, C., Lee, B. H., D'Ambro, E. L., Kurtén, T., & Thornton, J. A. (2016). Constraining the sensitivity of iodide adduct chemical ionization mass spectrometry to multifunctional organic molecules using the collision limit and thermodynamic stability of iodide ion adducts. *Atmospheric Measurement Techniques*, *9(4)*, 1505-1512. https://doi.org/10.5194/amt-9-1505-2016

Moncrieff, J., Clement, R., Finnigan, J., & Meyers, T. (2004). Averaging, detrending, and filtering of eddy covariance time series, In X. Lee, W. Massman & B. Law (Eds.), *Handbook of micrometeorology: A guide for surface flux measurement and analysis*, *Atmospheric and Oceanographic Sciences Library* (Vol. 29, pp. 7-31). Springer, Dordrecht.

Moncrieff, J. B., Massheder, J. M., De Bruin, H., Elbers, J., Friborg, T., Heusinkveld, B., Kabat, P., Scott, S., Soegaard, H., & Verhoef, A. (1997). A system to measure surface fluxes of momentum, sensible heat, water vapour and carbon dioxide. *Journal of Hydrology*, *188-189*, 589-611. https://doi.org/10.1016/S0022-1694(96)03194-0

Vickers, D., & Mahrt, L. (1997). Quality control and flux sampling problems for tower and aircraft data. *Journal of Atmospheric and Oceanic Technology*, *14(3)*, 512-526. https://doi.org/10.1175/1520-0426(1997)014<0512:QCAFSP>2.0.CO;2

Ye, C., Yuan, B., Lin, Y., Wang, Z., Hu, W., Li, T., Chen, W., Wu, C., Wang, C., & Huang, S. (2021). Chemical characterization of oxygenated organic compounds in the gas phase and particle phase using iodide CIMS with FIGAERO in urban air. *Atmospheric Chemistry and Physics*, *21(11)*, 8455-8478. https://doi.org/10.5194/acp-21-8455-2021